

The mass distribution of dwarf spheroidal galaxies from stellar kinematics: Draco, Ursa Minor and Fornax

Xiaoan Wu

Princeton University Observatory, Peyton Hall

Princeton, NJ 08544-1001, USA

xawn@astro.princeton.edu

ABSTRACT

We model three dSph galaxies, Draco, Ursa Minor and Fornax, as axisymmetric stellar systems embedded in spherical dark-matter potentials, which are in dynamical equilibrium without significant external tidal forces. We construct non-parametric two- and three-integral models that match the observed surface-density profiles and the current kinematic samples of $\sim 150\text{--}200$ stars per galaxy; these models naturally produce the so-called “extra-tidal extensions”, which had previously been suggested as evidence of tidal stripping. Isochrone, NFW and power-law models fit the data, but we strongly rule out any centrally condensed mass distribution like a dominant central black hole, as well as constant-density and (for Draco and Fornax) constant mass-to-light ratio models. The average V-band mass-to-light ratio is $400 \pm 80 \text{ M}_\odot/\text{L}_{V,\odot}$ within 0.75 kpc for Draco, $580^{+140}_{-100} \text{ M}_\odot/\text{L}_{V,\odot}$ within 1.1 kpc for Ursa Minor and $25^{+7}_{-5} \text{ M}_\odot/\text{L}_{V,\odot}$ within 2.5 kpc for Fornax. Two-integral models fit the data almost as well as three-integral models; in contrast to previous suggestions we do not find that anisotropy contributes substantially to the high mass-to-light ratios in these dSph galaxies.

Subject headings: Methods: statistical – galaxies: kinematics and dynamics – galaxies: fundamental parameters – galaxies: individual (Draco, Ursa Minor, Fornax) – cosmology: dark matter

1. Introduction

Dwarf galaxies include dwarf irregular (dIrr) and dwarf spheroidal (dSph) galaxies. Their luminosities ($10^3 - 10^8 L_\odot$, see e.g. Belokurov et al. 2007) are much smaller than the characteristic luminosity $L^* \sim 2 \times 10^{10} L_\odot$ for giant galaxies. The faintest dSph galaxies

have luminosities comparable to globular clusters, but are more extended (half-light radius ~ 0.5 kpc compared to ~ 0.005 kpc for globular clusters) and thus have much lower surface brightness.

The formation history of dwarf galaxies is not well-understood. The standard theory is that dwarf galaxies formed at the centers of subhalos orbiting within the halos of giant galaxies. However, the standard Λ CDM model predicts a much larger number of subhalos than the observed number of dwarf galaxies. There are ~ 50 known dwarf galaxies in the Local Group, compared to 300 predicted subhalos with circular velocity $\sim 10 - 20$ km s^{-1} (Klypin et al. 1999).

Aaronson (1983) was the first to determine the velocity dispersion of a dSph galaxy, using three stars in the Draco dwarf (6.5 km s^{-1}). Aaronson’s result was later confirmed by more extensive observations (Olszewski, Pryor & Armandroff 1996; Wilkinson et al. 2004). It is found that all dwarf galaxies have central velocity dispersions $\sim 6 - 25 \text{ km s}^{-1}$ (Mateo 1998). These dispersions are believed to reflect motions of the stars in the gravitational potential of the galaxy rather than (say) atmospheric motions or orbital motion due to a binary companion (Olszewski, Pryor & Armandroff 1996; Mateo 1998). If the systems are in dynamical equilibrium, the mass derived from these velocity dispersions is much larger than the stellar mass, resulting in a V-band mass-to-light ratio ranging from 7 to 500 $M_{\odot}/L_{V,\odot}$ (Irwin & Hatzidimitriou 1995; Wilkinson et al. 2002; Palma et al. 2003; Kleyna et al. 2005; Lokas et al. 2005). Therefore, dSph galaxies are probably the darkest objects ever observed in the universe, and thus provide unique probes of the dark-matter distribution on small scales.

Two possible alternatives to dark matter in dSph galaxies have been proposed. The first is Modified Newtonian Dynamics (MOND, Milgrom 1983). However, MOND has difficulty reproducing the different mass-to-light ratios of different dSph galaxies, mostly because MOND is based on a characteristic acceleration whereas the dSph galaxies seem to have a characteristic velocity dispersion instead. Moreover, MOND is difficult to reconcile with the power spectrum of fluctuations in the CMB (Spergel et al. 2006). The second alternative is tidal forces from the host galaxies. Tides have changed the structure and internal kinematics of the Sagittarius dwarf galaxy (Ibata, Gilmore & Irwin 1994; Ibata et al. 2001). So it is natural to postulate that other dSph galaxies are also undergoing tidal disruption, which leads to the high velocity dispersions (Kroupa 1997; Martínez-Delgado et al. 2001; Gómez-Flechoso & Martínez-Delgado 2003). However, (i) Sagittarius is much closer to the center of the Milky Way than other dwarf galaxies; (ii) tides should introduce strong velocity shear and dSph galaxies rotate slowly if at all; (iii) no mechanism of increasing velocity dispersions by tides appears to work for all dwarf galaxies (Mateo 1998; Klessen et al. 2003). There are

a few pieces of putative evidence that tides may influence the structure of Ursa Minor and Draco (Martínez-Delgado et al. 2001; Palma et al. 2003; Muñoz et al. 2005). For example, “extra-tidal extensions” (e.g., Irwin & Hatzidimitriou 1995; Wilkinson et al. 2004) are found beyond a “tidal radius” by fitting a King profile (King 1966) to stellar number density profiles. However, the King profile was intended to fit relaxed, constant mass-to-light ratio systems such as globular clusters (Trager et al. 1995), and perhaps the profile can not be applied to dSph galaxies.

In this paper we model the mass distribution of three dSph galaxies, specifically, Draco, Ursa Minor and Fornax. Since we focus on the inner parts (≤ 2 kpc) which are very regular (Irwin & Hatzidimitriou 1995) and not significantly affected by tidal stripping (Read et al. 2006), we assume that the inner part is in dynamical equilibrium with no significant external tidal forces, and test whether this assumption is self-consistent with a given mass distribution.

A wide variety of approaches have been used to model the kinematics of dSph galaxies. Different analysis techniques and assumptions have led to different results. Taking Draco as an example (see also Figure 4), if we calibrate the results assuming a V-band luminosity of $1.8 \times 10^5 L_\odot$ (Irwin & Hatzidimitriou 1995), Odenkirchen et al. (2001) derive a V-band mass-to-light ratio of $\bar{\Gamma}_V = 195 \pm 56 M_\odot/L_{V,\odot}$ within 1.2 kpc using a King model. Wilkinson et al. (2002) and Kleyna et al. (2002) assume parametric forms for both potential and distribution (hereafter DF), and model Draco as a near-isothermal sphere ($v_{circ} \propto r^{0.17}$), with $\bar{\Gamma}_V = 440 \pm 240 M_\odot/L_{V,\odot}$ within 0.7 kpc, more than a factor of two larger than derived by Odenkirchen et al. (2001) at a larger radius. By fitting velocity moments, Łokas (2002) investigates the dark matter distribution with parametric DFs and the assumption that dSph galaxies are spherical and derives $\bar{\Gamma}_V = 175 \pm 35 M_\odot/L_{V,\odot}$ within 0.4 kpc. Mashchenko, Sills & Couchman (2004) propose that the mass of Draco could range from 7×10^7 to $5 \times 10^9 M_\odot$, assuming an NFW (Navarro, Frenk & White 1997) potential, which has $\bar{\Gamma}_V = 540 \pm 170$ and 510 ± 160 at $r = 0.75$ and 1.1 kpc, respectively. Łokas et al. (2005) parametrize anisotropy by a constant anisotropy parameter β to fit velocity moments and found the mass-to-light ratio was $\sim 370 M_\odot/L_{V,\odot}$ and almost constant with radius for Draco. Wang et al. (2005) have determined dark matter distributions, using a sophisticated non-parametric mass distribution, assuming spherical symmetry. However, they assume that the distribution function is isotropic in velocity space, an assumption that can introduce much larger errors than the ones that are controlled by the use of non-parametric mass distribution. We believe that a better method is to use a non-parametric distribution function and a parametric potential.

The apparent ellipticities¹ of the stellar distributions of dSph galaxies vary from 0.13 (Leo II) to 0.56 (Ursa Minor) (Mateo 1998). However, the gravitational potential is dominated by the dark halo in these galaxies, and there is no reason to suppose that the dark halo shape is the same as the shape of the stellar distribution. Hence for simplicity, we assume that the galactic potential is spherical. In addition, we assume that the distribution of stars in the dSph galaxy is axisymmetric. Other methods designed to model axisymmetric galaxies (e.g., Cretton et al. 1999) are more general in that they allow both the potential and the distribution function to be axisymmetric; however, these are designed to work for a continuous, rather than discrete, observed distribution of stars. We describe and test our method in §2 and §3, respectively. Then we derive the mass density profiles for Draco, Ursa Minor and Fornax in §4. We discuss the results in §5 and conclude in §6.

2. Method

We introduce a Cartesian coordinate system, with origin at the center of the dwarf galaxy and z -axis along the line of sight. The x and y -axes are the apparent major and minor axes in the plane of the sky, respectively, which can be determined from isodensity contours of the surface number density profile (isopleths).

Then the distribution function may be written as $f(E, L, L_{z'})$, where E is energy, L is scalar angular momentum, the z' -axis is the intrinsic symmetry axis of the stellar distribution and $L_{z'}$ is the angular momentum along the z' -axis. Therefore, the z' -axis lies in the $y - z$ plane. For an observational data set of positions and line-of-sight velocities $\{x_i, y_i, v_{zi}\}$, we model $f(E, L, L_{z'})$ and determine both the parameters of the potential and the inclination θ , which is the angle between the z' -axis and the z -axis.

Wu & Tremaine (2006, hereafter Paper I) have used maximum likelihood analysis to deal with the analogous problem for spherically symmetric DFs in a spherical potential, where the DF is a function of two integrals, E and L . It is straightforward to generalize this method to the case of an axisymmetric DF $f(E, L, L_{z'})$. We define a probability function,

$$g(x, y, v_z) = \int f(E, L, L_{z'}) dv_x dv_y dz \quad (1)$$

which gives the probability density to observe a star at (x, y) with a line-of-sight velocity v_z . Note that g is also a function of θ and the assumed gravitational potential Φ . We maximize

¹If the apparent semi-major and minor axes of isopleths are a and b , then the apparent ellipticity $e_a = 1 - b/a$. Intrinsic ellipticity e_i is defined similarly, i.e., it is equal to e_a while the galaxy is seen edge-on.

the log likelihood function

$$LH(\Phi, f, \theta) = \sum_i \ln g(\{x_i, y_i, v_{zi}\} | \Phi, f, \theta), \quad (2)$$

assuming parametrized potentials and non-parametric DFs as follows.

For the potential, we assume an analytical form $\Phi(r, \mathbf{X})$ and infer the parameters \mathbf{X} . We investigate six possible forms.

1. An isochrone model,

$$\Phi(r) = -\frac{GM}{b + \sqrt{b^2 + r^2}}, \quad \mathbf{X} = \{M, b\}, \quad (3)$$

where M is the total mass.

2. The Navarro, Frenk & White (1997) density-potential pair,

$$\begin{aligned} \rho(r) &= \frac{\rho_n}{\frac{r}{r_n} \left(1 + \frac{r}{r_n}\right)^2}, \\ \Phi(r) &= -4\pi G \rho_n r_n^2 \frac{\ln \left(1 + \frac{r}{r_n}\right)}{\frac{r}{r_n}}, \end{aligned} \quad (4)$$

where r_n is the concentration radius and $\mathbf{X} = \{\rho_n, r_n\}$.

3. A power-law density-potential pair

$$\begin{aligned} \rho(r) &= \rho_0 \left(\frac{r}{r_0}\right)^{-\alpha}, \\ \Phi(r) &= \frac{4\pi G \rho_0 r_0^2}{(2-\alpha)(3-\alpha)} \left(\frac{r}{r_0}\right)^{2-\alpha} \quad (\alpha < 3), \end{aligned} \quad (5)$$

where r_0 is an arbitrary radius, and then $\mathbf{X} = \{\rho_0, \alpha\}$.

4. A constant-density model, which is a special case of the power-law model with $\alpha = 0$ and $\mathbf{X} = \{\rho_0\}$.
5. A constant mass-to-light ratio model (see §4.3).
6. A model in which the potential is dominated by a central black hole of mass M_{bh} ,

$$\Phi(r) = -GM_{bh}/r, \quad \mathbf{X} = \{M_{bh}\}. \quad (6)$$

For comparison with earlier analysis by other authors, we shall also fit the data using a more conventional method: fitting to the King (1966) three-parameter family of isotropic stellar systems, by minimizing χ^2 for the surface-density and velocity-dispersion profiles (see §4.2).

There is little rotation in dSph galaxies. Therefore, we do not attempt to model the observed rotation: we simply assume f is an even function of $L_{z'}$. Furthermore, the non-rotating model has even symmetry around the x and y -axes, i.e., $g(x, y, v_z) = g(|x|, |y|, |v_z|)$, so we can assume that x, y, v_z are all positive and $0 \leq \theta \leq \pi/2$. These simplifications increase the computational efficiency significantly.

To construct the DF, we divide the $\{E, L, |L_{z'}/L|\}$ space into $N_E \times N_L \times N_{z'}$ bins, which are denoted by the triple index mnl , $m = 1, \dots, N_E$, $n = 1, \dots, N_L$, $l = 1, \dots, N_{z'}$. The bins are mutually exclusive and cover all of the allowed $E - L - L_{z'}/L$ space, as well as some unallowed regions. In our calculation, bin mnl is defined by

$$E_{m-1} \leq E < E_m, \quad (7)$$

$$\frac{n-1}{N_L} L_c^2(E_m) \leq L^2 < \frac{n}{N_L} L_c^2(E_m), \quad (8)$$

$$\cos \gamma_{l-1} \geq \left| \frac{L_{z'}}{L} \right| > \cos \gamma_l, \quad \text{where} \quad \gamma_l \equiv \frac{ul\pi}{2N_{z'}}. \quad (9)$$

Here E_{m-1} and E_m are the lower and upper limits of the energy in the bin, and $L_c(E)$ is the maximum angular momentum at energy E , corresponding to a circular orbit. To achieve uniform spatial resolution for different potential models, we choose the boundaries of energy bins $\{E_m\}$ as the potentials at a set of evenly separated radii. The limits in $L_{z'}/L$ are chosen so that the resolution in γ , the angle between the z' -axis and the vector normal to the orbital plane (the orbital inclination) is uniform. Note that for spherical systems, the natural choice is uniform in $\cos \gamma$, not γ . However, when modeling flattened systems, this choice yields too few bins near $\gamma = 0$. The factor u determines the maximum value for γ and must be 1 for the bins to cover all allowed regions. However, it can be chosen to be < 1 to model a galaxy with very flat (disk-like) stellar part with higher computational efficiency.

Assuming that the DF is constant in bin mnl and zero elsewhere, we can calculate a probability distribution in (x, y, v_z) space (cf. Paper I),

$$g_{mnl}(x, y, v_z | \mathbf{X}, \theta) \propto \int_{\text{bin } mnl} dv_x dv_y dz. \quad (10)$$

we normalize each $g_{mnl}(x, y, v_z | \mathbf{X}, \theta)$ so that $\int g_{mnl}(x, y, v_z | \mathbf{X}, \theta) dx dy dv_z = 1$.

Assuming the non-negative weights in the bins are $\mathbf{W} = \{w_{mnl}\}$, we have

$$\begin{aligned} \sum_{m,n,l} w_{mnl} &= 1, \\ g(x, y, v_z) &= \sum_{m,n,l} w_{mnl} g_{mnl}(x, y, v_z), \\ LH(\mathbf{X}, \mathbf{W}, \theta) &= \sum_i \ln \left(\sum_{m,n,l} w_{mnl} g_{mnl}(\{x_i, y_i, v_{zi}\} | \mathbf{X}, \theta) \right), \end{aligned} \quad (11)$$

where LH is the log of the likelihood. Notice that $g(x, y, v_z)$ has been normalized since all $g_{mnl}(x, y, v_z)$ are normalized. For a fixed inclination θ and fixed potential specified by the parameters \mathbf{X} , we maximize $LH(\mathbf{X}, \mathbf{W}, \theta)$ with respect to \mathbf{W} , then vary \mathbf{X} and θ to search for a global maximum $LH(\mathbf{X}, \mathbf{W}, \theta)$. More generally, the posterior probability of (\mathbf{X}, θ) is given by

$$P(\mathbf{X}, \theta) \propto P_{\mathbf{X}} P_{\theta} \max_{\mathbf{W}} (P_{\mathbf{W}} e^{LH(\mathbf{X}, \mathbf{W})}), \quad (12)$$

where P_{θ} , $P_{\mathbf{X}}$ and $P_{\mathbf{W}}$ are prior probabilities. We use

$$P_{\theta} = \sin \theta, \quad (13)$$

corresponding to an isotropic distribution of orientations. Our rule for choosing $P_{\mathbf{X}}$ is to assign a uniform probability distribution for dimensionless parameters and a uniform probability distribution in log scale for dimensional parameters. We choose $P_{\mathbf{W}} = 1$ in this paper; that is, in contrast to Paper I we do not use regularization to smooth the DF (in Paper I, we found that the errors in derived potential parameters for samples of a few hundred stars were dominated by statistical noise rather than different regularization levels).

It is straightforward to account for observational errors in velocities and observational cuts on the sample volume in velocity and position on the sky (velocity cuts are normally applied to eliminate interlopers). The former is dealt with by convolving $g_{mnl}(x, y, v_z)$ with a Gaussian error profile. The latter requires us to normalize $g_{mnl}(x, y, v_z)$ within the cuts in velocity and position.

If the surface density of the kinematic sample is proportional to the overall surface density of stars, we use Equation (11). If not, the distribution of positions contains no information, so in the likelihood function we use the conditional probability

$$h(v_{zi} | x_i, y_i, \mathbf{X}, \theta) = \frac{g(x_i, y_i, v_{zi} | \mathbf{X}, \theta)}{\int g(x_i, y_i, v_z | \mathbf{X}, \theta) dv_z}. \quad (14)$$

In this paper, we use Equation (11) for the calculations in this paper.

An observed surface number density profile may be available for many more stars, over a larger survey area than the kinematic sample. We can easily add this as an additional constraint. Assume the apparent ellipticity of the stellar part is e_a , and that its surface number density profile along the x -axis is $\Sigma_{obs}(R_e)$ with error $\sigma_\Sigma(R_e)$, where R_e is the distance along the x -axis. We maximize the quantity

$$Q \equiv LH - \frac{1}{2}\chi^2, \quad (15)$$

$$\chi^2 = \sum_j \frac{(\Sigma(R_{ej}) - \Sigma_{obs}(R_{ej}))^2}{\sigma_\Sigma(R_{ej})^2}, \quad (16)$$

$$\begin{aligned} R(\phi, R_e) &= \frac{R_e}{\sqrt{\cos^2 \phi + \sin^2 \phi / (1 - e_a)^2}}, \\ \Sigma(R_e) &\propto \int \frac{g(R \cos \phi, R \sin \phi, v_z)}{\cos^2 \phi + \sin^2 \phi / (1 - e_a)^2} dv_z d\phi \\ &= \sum_{m,n,l} w_{mnl} \int \frac{g_{mnl}(R \cos \phi, R \sin \phi, v_z)}{\cos^2 \phi + \sin^2 \phi / (1 - e_a)^2} dv_z d\phi, \end{aligned} \quad (17)$$

where R is the projected distance from the origin to the ellipse defining the isopleth at an angle ϕ relative to the x -axis. In Equation 17, $\Sigma(R_e)$ is free to be scaled by an arbitrary constant factor to minimize χ^2 . For some systems (e.g., Draco), the available measured surface number density profile is averaged along concentric circles rather than isopleths, we need to simply set $e_a = 0$ in Equation (17).

3. Simulations

To test the algorithm in §2, we construct a dSph galaxy in a power-law potential with

$$\begin{aligned} r_0 &= 0.5 \text{ kpc}, \quad \theta = \frac{1}{4}\pi = 0.7854, \\ \mathbf{X} &= \{\rho_0, \alpha\} = \{8.5 \times 10^7 \text{ M}_\odot / \text{kpc}^3, 1.2\}, \\ f(E, L, L_{z'}) &= \left(e^{-(E-700)^2/200^2} + 0.06 e^{-(E-1650)^2/200^2} \right) e^{sL/L_c(E)} \left(\frac{L_{z'}}{L} \right)^{10}, \end{aligned} \quad (18)$$

where s is an anisotropy parameter and E is in units of $(\text{km s}^{-1})^2$. The DF is chosen so that the energy distribution is bimodal to challenge our algorithm.

Figure 1a shows the spatial distribution of 200 stars in the simulated galaxy with $s = 5$ (tangential anisotropy), which has $e_a \sim 0.3$. We use the algorithm in §2 with $(N_E, N_L, N_{z'}) = (15, 5, 15)$ and no additional surface density data. Accounting for the

prior probability of θ (eq. 13), θ is derived to be 0.90 ± 0.07 by fitting a Gaussian to the probability distribution in Figure 1b, which is consistent with the input value at the 1.6σ level. Figure 1c shows the probability distribution of potential parameters, specifically, $\mathbf{X} = \{(8.1 \pm 1.2) \times 10^7 \text{M}_\odot/\text{kpc}^3, 1.17 \pm 0.25\}$. The triangle and plus sign are the input model and the best-fit model, respectively, which agree within the 1σ error. Therefore, our algorithm can recover both potential parameters and inclination.

Contrastingly, with the assumption that the stellar density is spherical and the DF is isotropic, i.e., $(N_E, N_L, N_{z'}) = (15, 1, 1)$, we may get large systematic errors. We have explored two cases. For the above input model with $s = 5$ (tangential anisotropy), the assumption leads to the best-fit model marked by the square with error bars in panel (d) of Figure 1. For another input model with $s = -5$ (radial anisotropy) and the same input potential ρ_0, α , the best-fit model marked by the cross is also inconsistent with the input model. We conclude that three-integral models that allow for both velocity anisotropy and flattening must be used to avoid possible systematic errors in the derived potential parameters.

For a face-on galaxy ($e_a = 0$), we find that the 2σ contour for potential parameters extends over at least two orders of magnitude in ρ_0 . Because the line-of-sight velocity dispersion is decoupled from the mass distribution for a face-on disk-like galaxy, an apparently round galaxy may be either a low-density spherical galaxy or a face-on high-density flat galaxy. Therefore, we get a poor constraint on potential parameters of an apparent round dSph galaxy. In practice, we never see disk-like dSph galaxies, so when modeling a galaxy with $e_a = 0$ we will not make a serious error by assuming that the stellar distribution is spherical and using the analogous methods described in Paper I for spherical systems of test particles². This is not an issue for the three galaxies analyzed in this paper, which are sufficiently flattened that they yield well-constrained results for the potential parameters and inclination.

4. Application to Draco, Ursa Minor and Fornax

4.1. Data

Our algorithm is applied to kinematic data $\{x, y, v_z\}$ and number density profiles $\Sigma_{\text{obs}}(R_e)$ of three dSph galaxies taken from the published literature. Table 1 lists several parameters

²On the other hand, for a flat edge-on galaxy ($e_a = 1.0$), the intrinsic ellipticity e_i is also 1.0, so we may overestimate the mass by up to 50% if assuming that the stellar distribution is spherical ($f = f(E, L)$).

of each galaxy, including the assumed heliocentric distance (D), the luminosity in the V-band (L_V), apparent ellipticity (e_a), and the position angle of the major axis derived from the isopleths, as usual measured eastward from north (PA). In the kinematic sample, we include N_k stars, which have heliocentric velocities in the range $v_k \pm \Delta v$ and are inside an ellipse with semi-major axis R_k and ellipticity e_a , to exclude possible interlopers which could strongly bias the results (the same cuts are applied to our likelihood distribution, so this procedure introduces no systematic errors). Table 1 also lists the number of stars (N_s) and annuli (N_a) in the surface number density profile $\Sigma_{obs}(R_e)$, which has a maximum radius R_m . For the outer parts ($R > R_g$), where the number density is very low, we combine a few annuli to increase the signal-to-noise ratio. For Draco, we exclude two bins in which the number density is more than 3σ away from those in nearby bins.

4.2. King model

Since King models are spherical, we convert the elliptical surface density distribution to a spherical one, with a surface number density profile

$$\Sigma'(R') = \Sigma_{obs}(R_e), R' = \sqrt{1 - e_a} R_e, \quad (19)$$

so that the number of stars enclosed in a circle with radius R' and an ellipse with semi-major axis R are equal. A King model is defined by three parameters, which may be chosen as the characteristic velocity dispersion of the DF σ , the difference between the potential at the tidal radius and that at the center $\Phi(0)$ in units of σ^2 , and a core radius r_c (see Binney & Tremaine 1987, for details). Since the DF is parametric, we do not use the method in §2, but fit velocity dispersion profiles and number density profiles, as shown in Figure 2. We have binned the kinematic data into $N_b = 10$ bins with approximately the same number of stars in each bin. Considering the likelihood and assigning a flat prior probability for $\{\Phi(0)/\sigma^2, \ln \sigma\}$, we estimate the parameters and their errors, which are given in Table 2.

We fit the observed line-of-sight velocity dispersion profiles while Irwin & Hatzidimitriou (1995), having a smaller kinematic data set, only fit the core radial velocity dispersion. Moreover, Irwin & Hatzidimitriou (1995) estimate an average velocity dispersion 7.5 ± 1.0 km s⁻¹ from 46 stars for Ursa Minor, which is much lower than 13.3 ± 0.4 km s⁻¹ from 163 stars used in our calculation. Nonetheless, considering the factor of 2.0 in the velocity dispersion for Ursa Minor, the derive mass-to-light ratios (see Table 2) similar to the values of Irwin & Hatzidimitriou (1995), $\bar{\Gamma}_V = 245 \pm 155$ M_⊙/L_{V,⊙} for Draco, 95 ± 43 M_⊙/L_{V,⊙} for Ursa Minor and 7 ± 3 M_⊙/L_{V,⊙} for Fornax.

Figure 2 shows that a single-component King model does not fit the data of Draco

and Fornax, but is formally consistent with those of Ursa Minor. However, the last point of the Ursa Minor kinematic data suggests that a King model may be ruled out if future observations show that the flat dispersion profile extends to larger radii. In all three systems, the observational data have an excess in both velocity dispersion and surface number density at large radii, and the dispersion profile is flat rather than decreasing as in the King models.

4.3. More general models

We fit the parametrized models for the mass distribution in §2 to the data. We must assume a maximum radius R_{max} , so that the upper energy limit of the bins in Equation (7) is $\Phi(R_{max})$. We set R_{max} as 2 kpc for Draco and Ursa Minor, 6 kpc for Fornax, which are reasonable because the surface number density is negligible at these radii. For the power-law model, we set r_0 as 0.28 kpc for Draco, 0.6 kpc for Ursa Minor and 1.1 kpc for Fornax to minimize the covariance of ρ_0 and α in their bivariate probability distribution.

The models labeled “constant mass-to-light ratio” require some explanation. Since our method assumes that the potential is spherical in this paper, we do not attempt to construct a full model of a non-spherical galaxy with constant mass-to-light ratio. To derive the potential of the constant mass-to-light-ratio model, we assume that all stars have the same mass-to-light ratio and construct a spherical density distribution as in Equation (19). So the luminosity profile $\nu_s(r)$ is proportional to the volume number density of stars. The spherical assumption is then used to derive the potential, but dropped when modeling the galaxy itself, i.e., we assume a non-spherical galaxy in a spherical potential.

It is convenient to fit luminosity profile ν_s with a linear combination of two exponential functions

$$\nu_s(r) = \begin{cases} ae^{-br} + ce^{-dr} & , r < R_{max} \\ 0 & , r \geq R_{max}, \end{cases} \quad (20)$$

where a, b, c, d are constant parameters listed in Table 3 so that

$$L_V = 4\pi \int_0^{R_{max}} \nu_s(r) r^2 dr. \quad (21)$$

The chi-square of the fitting shows that the luminosity profiles are indeed well approximated by Equation (20).

This density distribution gives a potential

$$\Phi(r) = -4\pi G \bar{\Gamma}_V \left(\frac{a(2/r - e^{-br}(b + 2/r))}{b^3} + \frac{c(2/r - e^{-dr}(d + 2/r))}{d^3} \right). \quad (22)$$

The potential is dependent on $\mathbf{X} = \{\bar{\Gamma}_V\}$, the constant mass-to-light ratio in the V-band.

We consider two types of models, those with $N_L = 1$, and $N_E, N_{z'} \gg 1$, which correspond to models having $f = f(E, L_{z'})$ (two-integral models), and those with all of $N_L, N_E, N_{z'} \gg 1$ (three-integral models). The two-integral models are much faster to compute and appear to fit the data just as well as the three-integral models for the three dSphs, so we focus on the two-integral models.

4.4. Results

4.4.1. Two integral models ($N_L = 1$)

Table 4 lists the results for various models with $(N_E, N_L, N_{z'}) = (15, 1, 20)$, the difference in log likelihood ΔLH , potential parameters \mathbf{X} , mass and mass-to-light ratio within $r = R_k$ (see Table 1). To determine the uncertainties in the derived parameters, we lay down points with a uniform probability distribution in $\ln(\mathbf{X})$ if \mathbf{X} is dimensional and in \mathbf{X} otherwise, then reject or save each point according to the likelihood at that point. From the saved points, we may estimate the model parameters and their errors. In practice, we consider a set of discrete values for θ ,

$$\theta = \frac{i\pi}{20}, \quad \frac{20}{\pi} \arccos(e_a) < i \leq 10. \quad (23)$$

where i is a natural number. For all models of the three dwarf spheroidals, either $i = 9$ or 10 gives the maximum $P(\mathbf{X}, \theta)$ and others give much smaller likelihoods (3σ away). Therefore, we do not try to fit θ accurately, but give a rough estimate $\theta \sim 1.45 \pm 0.12$.

Several features of Table 4 are worth noting: (i) For the NFW and isochrone models, there is a strong correlation between the two parameters in \mathbf{X} , which explains why the fractional error in $M(r < R_k)$ is smaller than the fractional error in the potential parameters. (ii) The best-fit isochrone, NFW and power-law models have $-4.2 \leq \Delta LH < 0$, corresponding to $< 2.9\sigma$. The models of a dominant central black hole, constant density and (for Draco and Fornax) constant mass-to-light ratio are less likely at $> 3.7\sigma$ levels. (iii) The difference in log likelihood only indicates the relative likelihood among different models, so it is important to investigate whether the best-fit model is a good fit. In Figure 3 we show the observed velocity dispersion $\sigma_{v,obs}(R)$ in ten bins (top row). For the stars in a bin centered at R , say, $\{x_j, y_j, v_{zj}\}$, we calculate the predicted velocity dispersion $\sigma_{v,fit}(R)$ from the velocity distribution profile

$$h(v_z|R) = \sum_j g(x_j, y_j, v_z). \quad (24)$$

Comparison of the first two rows of panels in Figures 2 and 3 shows that the present models provide a substantially better fit to the observed velocity-dispersion and surface-density profiles in all three galaxies than the best-fitting King models. This visual impression is confirmed in Table 6, which gives goodness-of-fit statistics for the velocity-dispersion profile (χ_v^2) and surface-density profile (χ^2) and their deviations from the expected values N_b and N_a (the number of bins), in units of the standard deviation $\sqrt{2N_b}$ or $\sqrt{2N_a}$ (1σ error). The deviations for the present models are $< 2.1\sigma$ for all three galaxies, while the King models are much poorer fits for Draco and Fornax. (iv) Note that the models are fitted to the surface-density distribution as a function of radius, assuming the observed ellipticity e_a (eqs. 14-17). Thus it is not guaranteed that the ellipticity of the isopleths in the models will be similar to the observed ellipticity (no doubt a better approach would have been to fit the two-dimensional surface-density distribution, but this is substantially more computationally expensive). Nevertheless the ellipticities of the models, quoted in Table 6 at the core radius, are similar to the observed ellipticities.

The third row in Figure 3 shows the derived mass profiles of various models for the three dSph galaxies. All of the models shown are within 2.5σ of the best-fit models. The models have similar density distributions at intermediate radii, for example, $0.25 - 1.0$ kpc for Draco, but (not surprisingly) differ substantially at radii beyond the outermost observational data. To summarize, our algorithm gives relatively small errors at intermediate radii, and the surface number density profile only weakly constrains the mass density profile beyond $r = R_k$.

The bottom row in Figure 3 shows the average mass-to-light ratio $\bar{\Gamma}_V(r)$ for the best-fit models. The light inside a radius r is calculated from Equation (20). Comparing Table 2 and 4, we can see that King model gives estimates of mass at the outer limit of the kinematic data, $r = R_k$, consistent with those from more general models within 2σ . However, King model assumes a constant mass-to-light ratio, which is an average value. For the more general models, except at small radii where the mass density is very uncertain, the mass-to-light ratios increase with radius. Therefore, the global mass-to-light ratios are probably even greater than $\bar{\Gamma}_V(R_k)$.

4.4.2. Three integral models ($N_L = 5$)

We have shown that two integral ($N_L = 1$) models can reproduce all of the observed features of dSph galaxies. We also list the results for three-integral models, $(N_E, N_L, N_{z'}) = (15, 5, 20)$, in Tables 5 and 6. The mass-to-light ratios are generally larger than the values for $N_L = 1$ models by 10% to 50%. This result suggests that given the freedom to adjust

the DF in L direction, high mass models are better able to fit the observed data than low mass models, thus the derived mass distributions are more skewed to the high end. In the following sections, we adopt the conservative (lower) estimates of mass-to-light ratios that are derived with the case of $N_L = 1$.

5. Discussion

We believe that the mass estimates presented here are the most accurate and reliable that have so far been obtained for the three dSph galaxies, Draco, Ursa Minor and Fornax. In our models, we assume that the stellar distributions are not significantly affected by the tidal force of the Milky Way. This assumption is confirmed by a dynamical argument: using the mass $M(r < R_k)$ of the best-fit models in Table 4, which is a lower limit to the total mass, the Roche limit is 2.6 kpc ($3.5R_k$) for Draco, 2.6 kpc ($2.4R_k$) for Ursa Minor and 6.6 kpc ($2.4R_k$) for Fornax, assuming that the Milky Way is an isothermal sphere with $v_{\text{circular}} = 220 \text{ km s}^{-1}$. The Roche limits also exceed R_{max} , the maximum radius used in our dynamic models in §4.3. Therefore, our assumption that the dSph galaxies are isolated systems in virial equilibrium is self-consistent. Because our models can fit both radial velocity profiles and surface number density profiles, the so-called “extra-tidal extensions” in the surface number density profiles found by Irwin & Hatzidimitriou (1995) and Wilkinson et al. (2004) do not require any special ad hoc explanation. Thus it is not valid to consider them as the evidence of tidal stripping, as proposed by some authors (e.g., Martínez-Delgado et al. 2001; Gómez-Flechoso & Martínez-Delgado 2003; Muñoz et al. 2005).

We strongly rule out any centrally condensed mass distribution like a dominant central black hole, as well as constant-density and (for Draco and Fornax) constant mass-to-light ratio models. For example, the constant-density model is ruled out at the level of 4.1σ for Draco, 3.4σ for Ursa Minor and 4.4σ for Fornax. In contrast to the positive result of Łokas et al. (2005) based on the same data set, the constant mass-to-light ratio is ruled out at 8.6σ level for Draco.

We derive an average mass-to-light ratio of $400 \pm 80 \text{ M}_\odot/\text{L}_{V,\odot}$ within 0.75 kpc for Draco, $580^{+140}_{-100} \text{ M}_\odot/\text{L}_{V,\odot}$ within 1.1 kpc for Ursa Minor and $25^{+7}_{-5} \text{ M}_\odot/\text{L}_{V,\odot}$ within 2.5 kpc for Fornax. Note that these values are probably lower limits for the global mass-to-light ratio because the mass-to-light ratio increases with r for the best-fit models. The mass-to-light ratios we obtain for all three galaxies are larger than the estimates of global mass-to-light ratio by Irwin & Hatzidimitriou (1995) ($245 \pm 155 \text{ M}_\odot/\text{L}_{V,\odot}$ for Draco, $95 \pm 43 \text{ M}_\odot/\text{L}_{V,\odot}$ for Ursa Minor and $7 \pm 3 \text{ M}_\odot/\text{L}_{V,\odot}$ for Fornax). The discrepancies arise because the results of Irwin & Hatzidimitriou (1995) and Odenkirchen et al. (2001) are based on a single-component King

model and because we have a larger sample of radial velocities, covering a larger range of radii.

Figure 4 shows the derived mass-to-light ratio of Draco as a function of radius and the estimates by other authors. The mass-to-light ratio for Draco is assumed constant in some of these studies (Irwin & Hatzidimitriou 1995; Lokas et al. 2005) but is allowed to vary with radius in others (Odenkirchen et al. 2001; Lokas 2002; Kleyna et al. 2002; Mashchenko, Sills & Couchman 2004). Piatek et al. (2002) have proposed that the large mass-to-light ratios of dSph’s may be partly due to velocity anisotropy, since anisotropy can inflate the derived $\bar{\Gamma}_V$ by a factor of three or so if the kinematic information is restricted to the central parts of the galaxy. The simulations of §3 confirm that velocity anisotropy and flattening of the stellar distribution (i.e., the dependence of the DF on L and $L_{z'}$) must be accounted for to obtain accurate mass-to-light ratios. Nonetheless, for the three dSph galaxies, the DF $f(E, L_{z'}/L)$ fits the data reasonably well (§4.4), and the derived masses actually increase if we allow the dependence of DF on L (§4.3). So we find no evidence that three-integral models fit the current data significantly better than two-integral models, or that they prefer models with lower mass-to-light ratio.

Wilkinson et al. (2004) and Kleyna et al. (2004) argue that the velocity dispersion profiles of Draco and Ursa Minor seem to show a sharp drop at radii of 0.81 and 0.84 kpc, respectively. The drop in the dispersion profile seems to coincide with a “break” in the number density profile, and Wilkinson et al. propose that this is evidence of a kinematically cold population. However, the sharp drop may only be present in particular binning schemes (Muñoz et al. 2005) and is not seen with our binning scheme (Figure 2). Our models do not reproduce such a sharp drop. Thus, the drop is inconsistent with stationary axisymmetric models of the DF and also is not statistically significant given the present data.

The large masses that we have derived may help alleviate but may not eliminate the problem that there are far fewer dwarf galaxies in the Local Group than predicted by standard cosmological models.

6. Conclusion

We model dSph galaxies as axisymmetric stellar systems in spherical potentials, which are in dynamical equilibrium without significant external tidal forces. For the three dSph galaxies, Draco, Ursa Minor and Fornax, plausible parametric models of the potential combined with non-parametric two-integral models of the stellar distribution function can naturally reproduce the observed velocity dispersion profiles and number density profiles. The

masses of these models are high enough so that tidal forces from the Milky Way do not significantly affect the observed kinematics. So the models are self-consistent and “extra-tidal extensions” simply reflect an extended axisymmetric envelope that is still in virial equilibrium. The sharp drop in velocity dispersion which coincides with a “break” in the light distribution that has been claimed in the literature is not observed in our binning scheme and can not be reproduced in the scenario of virial equilibrium.

The isochrone, NFW and power-law models all fit the data. We strongly rule out any centrally condensed mass distribution like a dominant central black hole, as well as constant-density and (for Draco and Fornax) constant mass-to-light ratio. The average V-band mass-to-light ratio in our best-fit two-integral models is $400 \pm 80 \text{ M}_\odot/\text{L}_{V,\odot}$ within 0.75 kpc for Draco, $580^{+140}_{-100} \text{ M}_\odot/\text{L}_{V,\odot}$ within 1.1 kpc for Ursa Minor and $25^{+7}_{-5} \text{ M}_\odot/\text{L}_{V,\odot}$ within 2.5 kpc for Fornax. Our method considers both anisotropy of the DF and the non-spherical geometry of the stellar population, and investigates a large variety of mass distribution models, and thus should yield more reliable mass distributions than previous investigations.

Our simulations show that anisotropy (dependence on L) and flattening (dependence on $L_{z'}$) in the DF may substantially affect derived masses of axisymmetric galaxies. However, we detect no strong evidence of anisotropy in the three dSph galaxies, i.e., a two-integral DF $f(E, L_{z'})$ is consistent with the data. Allowing anisotropy yields even larger mass-to-light ratios.

Our method could be improved by fitting the two-dimensional surface number-density distribution rather than a one-dimensional profile. Observationally, it would be useful to extend the kinematic surveys to larger radii, since the current limits are still well within the radii where tidal forces are likely to complicate the analysis.

I thank Scott Tremaine for numerous stimulating discussions and helpful comments on an earlier draft, James Gunn, David Spergel, Michael Strauss and Glenn van de Ven for helpful discussions. I wish to thank Mark Wilkinson for providing the kinematic data of Draco and Ursa Minor and surface number density profile of Draco in tabular form. This research was supported in part by NASA grant NNG04GL47G and used computational facilities supported by NSF grant AST-0216105.

REFERENCES

- Aaronson, M., 1983, ApJ, 266, L11
 Belokurov, V., 2007, ApJ, 654, 897

- Binney, J., & Tremaine S., 1987, *Galactic Dynamics*, Princeton University Press
- Cretton, N., De Zeeuw, P. T., van der Marel, R. P., & Rix, H.-W., 1999, *ApJ*, 124, 383
- Gomez-Flechoso, M. Á., Fux, R. & Martinet, L., 1999, *Å*, 347, 77
- Gómez-Flechoso, M. Á, & Martínez-Delgado, D., 2003, *ApJ*, 586, L123
- Ibata, R. A., Gilmore, G., & Irwin, M. J., 1994, *Nature*, 370, 194
- Ibata, R., Irwin, M., Lewis, G. F., & Stolte, A., 2001, *ApJ*, 547, L133
- Irwin, M., & Hatzidimitriou, D., 1995, *MNRAS*, 277, 1354
- King, I. R., 1966, *AJ*, 71, 1
- Klessen, R. S., Grebel, E. K., & Harbeck, D., 2003, *ApJ*, 589, 798
- Kleyana, J., Wilkinson, M. I., Evans, N. W., Gilmore, G., & Frayn, C., 2002, *MNRAS*, 330, 792
- Kleyana, J. T., Wilkinson, M. I., Evans N. W., & Gilmore, G., 2004, *MNRAS*, 354, L66
- Kleyana, J. T., Wilkinson, M. I., Evans N. W., & Gilmore, G., 2005, *ApJ*, 630, L141
- Klypin, A., Kravtsov, A. V., & Valenzuela, O., 1999, *ApJ*, 522, 82
- Kroupa, P., 1997, *New A*, 2, 139
- Lokas, E. L., 2002, *MNRAS*, 333, 697
- Lokas, E. L., Mamon, G. A., & Prada, F., 2005, *MNRAS*, 363, 918
- Martínez-Delgado, D., Alonso-García, J., Aparicio, A., & Gómez-Flechoso, M. A., 2001, *ApJ*, 549, L63
- Mashchenko, S., Sills, A., & Couchman, H. M. P., 2006, *ApJ*, 640, 252
- Mateo, M., 1998, *ARA&A*, 36, 435
- Milgrom, M., 1983, *ApJ*, 270, 365
- Muñoz, R., Frinchaboy, P. M., Majewski, S. R., Kuhn, J. R., Chou, M.-Y., Palma, C., Sohn, S. T., Patterson, R. J., & Siegel, M. H., 2005, *ApJ*, 631, L137
- Navarro, J. F., Frenk, C. S., & White, S. D. M., 1997, *ApJ*, 490, 493

- Odenkirchen, M., et al., 2001, *AJ*, 122, 2538
- Olszewski, E. W., Pryor, C., & Armandroff, T. E., 1996, *AJ*, 111, 2
- Palma, C., Majewski, S. R., Siegel, M. H., Patterson, R. J., Ostheimer, J. C., & Link, R., 2003, *ApJ*, 123, 1352
- Piatek, S., Pryor, C., Armandroff, T. E., & Olszewski, E. W., 2002, *ApJ*, 123, 2511
- Read, J. I., Wilkinson, M. I., Evans, N. W., Gilmore, G., & Kleyna, J., 2006, *MNRAS*, 367, 387
- Spiegel, D. et al., 2006, *astro-ph/0603449*
- Trager, S. C., King I. R., & Djorgovski, S., 1995, *AJ*, 109, 1
- Wang, X., Woodroffe, M., Walker, M. G., & Mateo, M., 2005, *ApJ*, 626, 145
- Walker, M. G., Mateo, M., Olszewski, E. W., Bernstein, R. A., Wang, X., & Woodroffe, M., 2006, *AJ*, 131, 2114
- Wilkinson, M. I., Kleyna, J., Evans, N. W., & Gilmore G., 2002, *MNRAS*, 330, 778
- Wilkinson, M., Kleyna, J. T., Evans, N. W., Gilmore, G. F., Irwin M. J., & Grebel, E. K., 2004, *ApJ*, 611, L21
- Wu, X., & Tremaine, S., 2006, *ApJ*, 643, 210

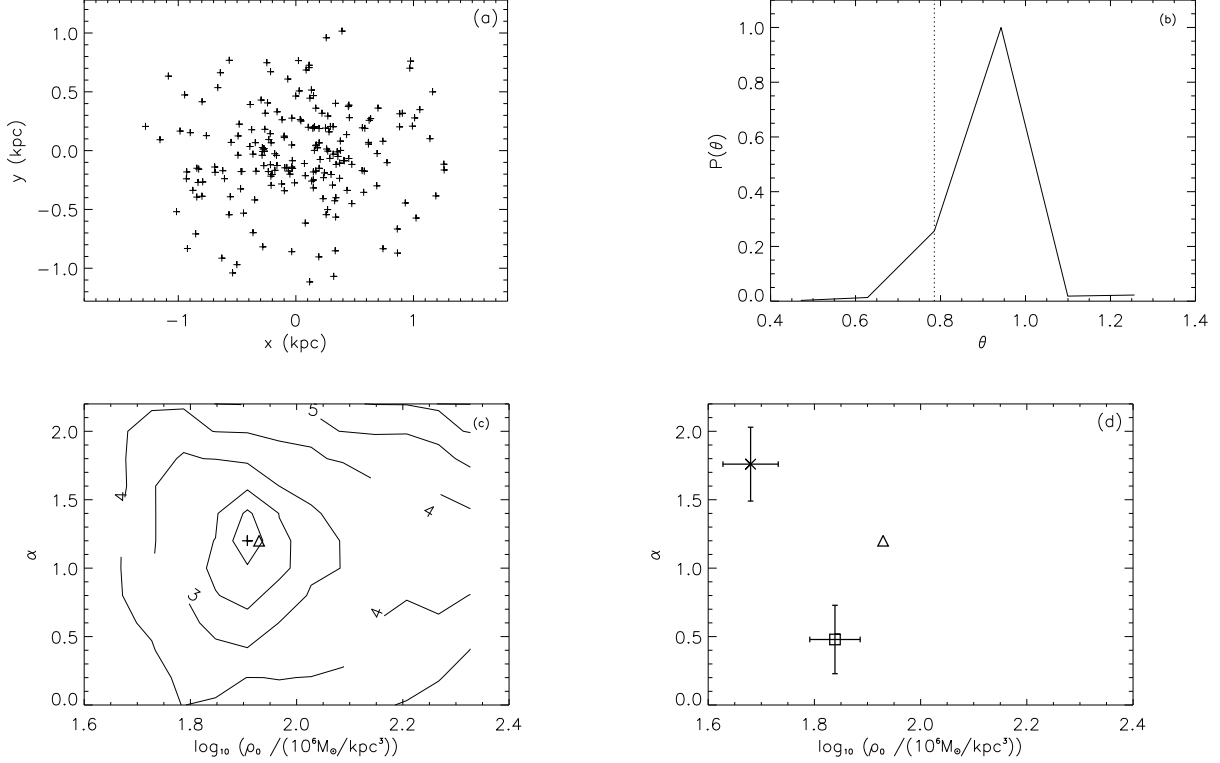


Fig. 1.— Algorithm tests. (a) A test dSph galaxy with 200 observed stars, described by Equation (18) with $s = 5$ (tangential anisotropy). (b) Probability distribution of θ derived from the 200 stars. The input value is marked by the dotted line. (c) Likelihood contours for the potential parameters. The contours are $n\sigma$ levels from the peak, i.e., $e^{-n^2/2}$ of the maximum likelihood. The triangle is the input model and the plus sign is the best-fit model with $(N_E, N_L, N_{z'}) = (15, 5, 15)$. They agree within 1σ error. (d) This panel shows the results of fitting flattened anisotropic galaxies with spherical, isotropic models. The triangle is the input model which is the same model described in (a) except that s can be $+5$ or -5 (radial anisotropy). The square with error bars is the best fit for the model with $s = 5$, assuming that the stellar part is spherical and the DF is isotropic, $(N_E, N_L, N_{z'}) = (15, 1, 1)$, while the cross is the same as the square except for the input model with $s = -5$. The large errors in the recovered potential parameters show that both anisotropy of the DF and non-spherical geometry of the stellar population should be accounted for whenever their effects may be significant.

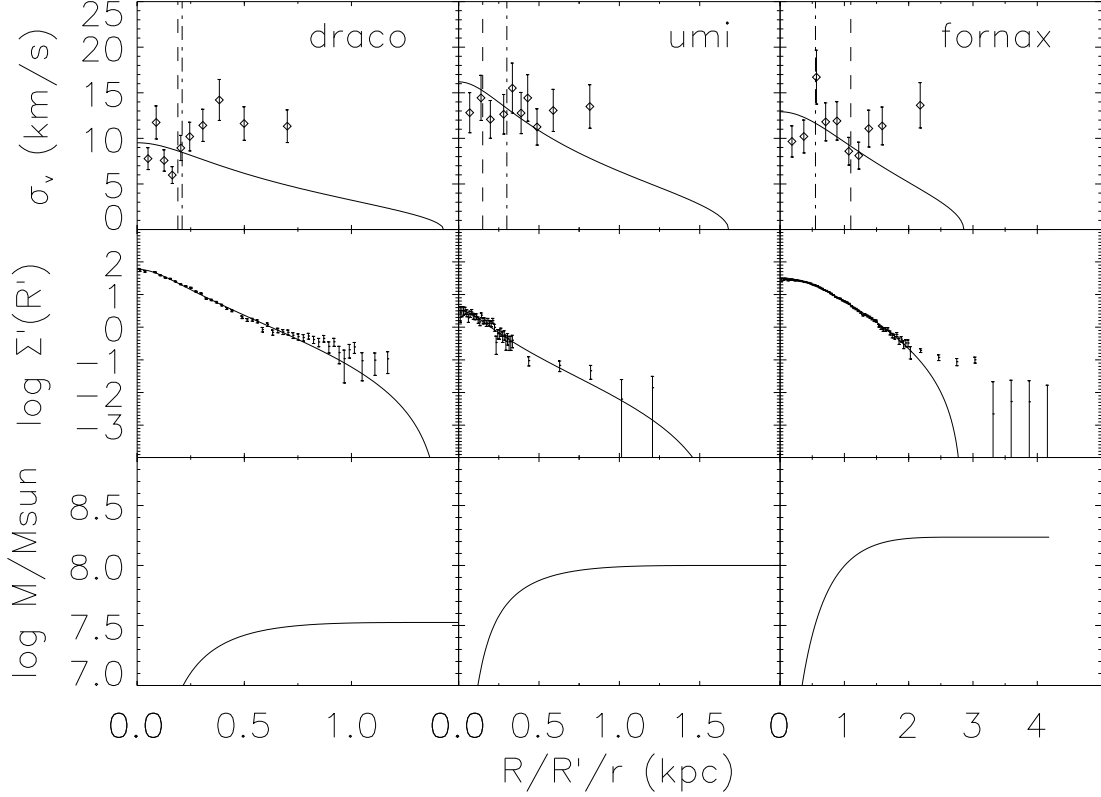


Fig. 2.— Fitting King models to dSphs. The upper row shows the observed and best-fit velocity dispersion profiles $\sigma_{v,obs}$ (points with error bars) and $\sigma_{v,fit}$ (solid lines). Also shown are the derived core radii (dashed lines) and those from Irwin & Hatzidimitriou (1995) (dash-dotted lines). The middle row shows the observed density profiles ($\Sigma'(R')$, eq. 19) and the best-fit. The bottom row shows the mass profiles of the best-fit King models. The core radius r_c is 0.19 kpc for Draco, 0.15 kpc for Ursa Minor and 1.10 kpc for Fornax. A single-component King model does not fit the data of Draco and Fornax, but is consistent with those of Ursa Minor. However, in all three galaxies the model shows a decline of velocity dispersion with radius that is not seen in the data.

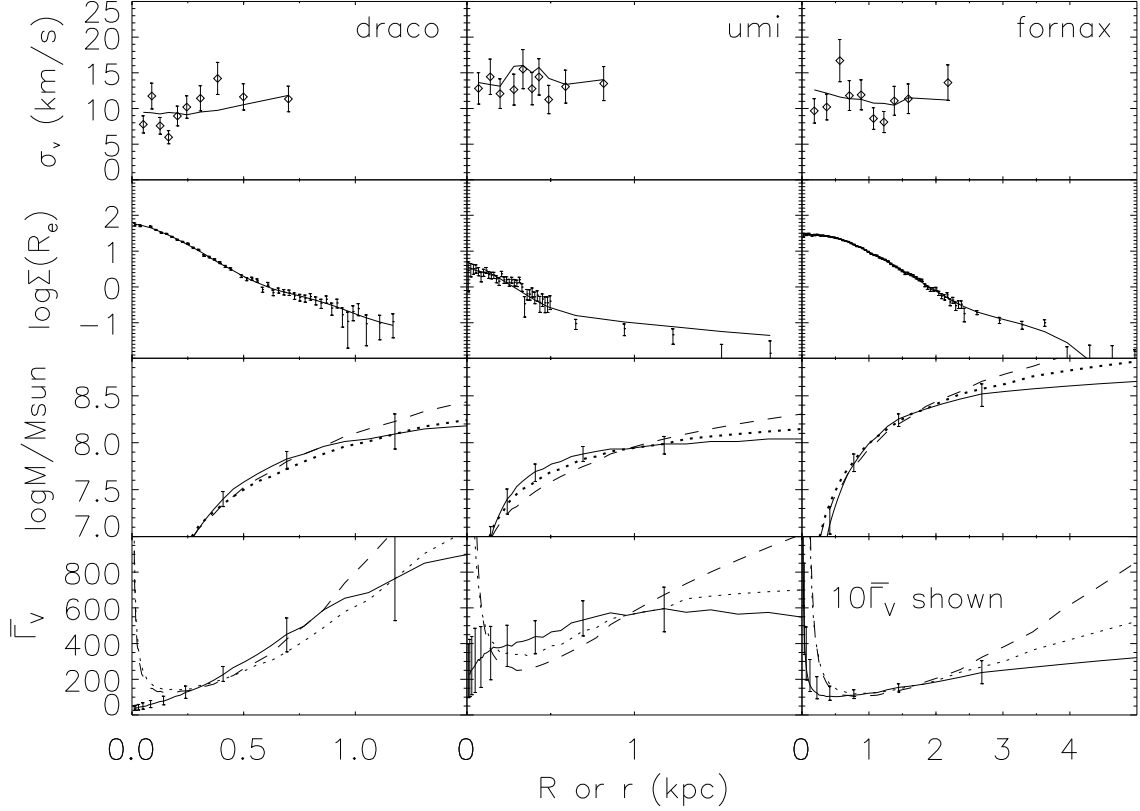


Fig. 3.— Best-fit two integral models ($N_L = 1$) for three dSph galaxies. Top row: observed velocity dispersion profiles $\sigma_{v,obs}(R)$ and those of the best-fit models $\sigma_{v,fit}(R)$ (see eq. 24). Also shown are the core radius r_c (dotted lines) and kinematic survey radius R_k (dashed lines). Second row: observed surface number density profiles $\Sigma_{obs}(R_e)$ and those of the best-fit models. Third row: derived mass profiles for the isochrone (solid lines), NFW (dotted lines) and power-law models (dashed lines). All three models agree relatively well at intermediate radii. Bottom row: derived average mass-to-light ratio within radius r . For Fornax, $\bar{\Gamma}_v$ has been multiplied by a constant 10.0 for clear presentation. The mass-to-light ratios tend to increase with r except at small radii, where the mass density is very uncertain.

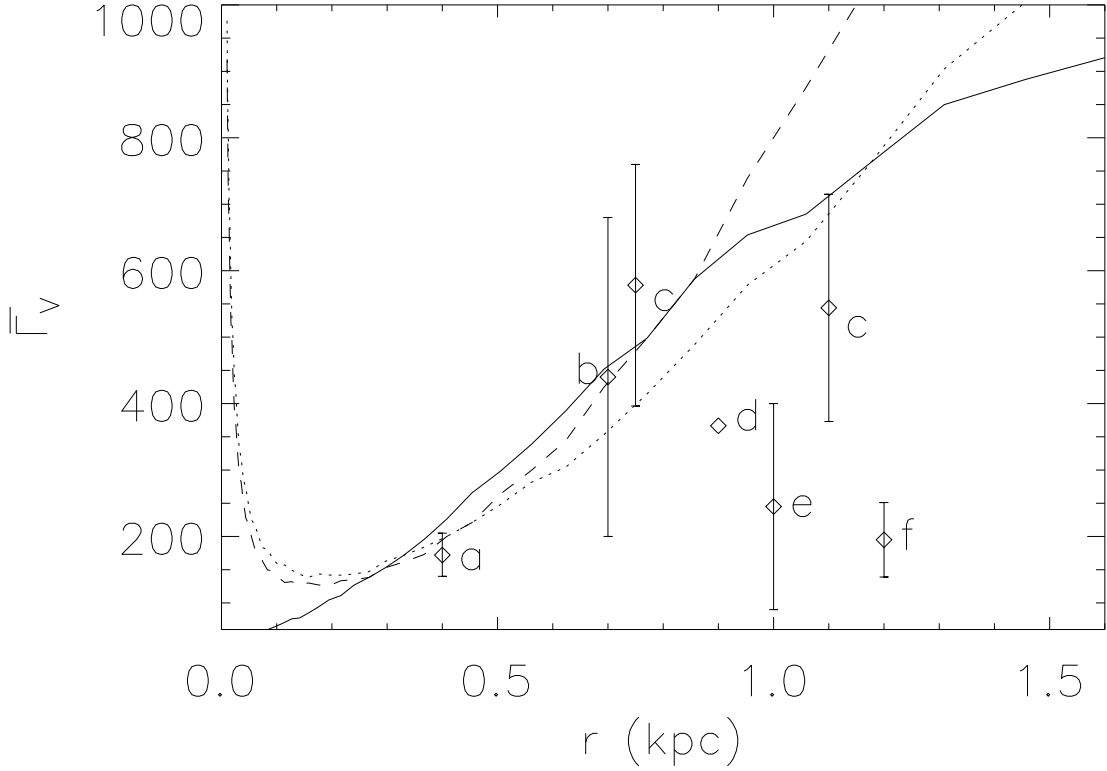


Fig. 4.— Derived mass-to-light ratio for the best-fit isochrone (solid line), NFW (dotted line) and power-law (dashed line) models for two-integral models ($N_L = 1$) for Draco. Also plotted are measurements by a: Łokas (2002) b: Kleyna et al. (2002) c: Mashchenko, Sills & Couchman (2004) d: Łokas et al. (2005) e: Irwin & Hatzidimitriou (1995), f: Odenkirchen et al. (2001). The average mass-to-light ratio r is assumed constant over r in references d and e but is an estimate at the radii shown for other measurements.

Table 1. Data summary^a

	Draco	Ursa Minor	Fornax	Reference
galaxy parameters				
D (kpc)	82	66	138	1
L_V ($10^5 L_{V,\odot}$)	1.8	2.0	140	1, 2
e_a	0.29	0.56	0.30	2
PA (degree)	88	56	41	2, 3
kinematic data				
N_k	197	163	147	4, 5
$v_k \pm \Delta v$ (km s ⁻¹)	-290.7±30.0	-245.2±35.0	53.3±30.0	...
R_k (kpc)	0.75	1.1	2.5	...
surface number density profiles				
N_s	18000	1500	42000	2, 4
R_m (kpc)	1.2	1.3	4.0	...
R_g (kpc)	n/a	0.5	2.5	...
N_a	44	38	66	...

^aSee section §4.1 for explanations of the parameters.

References. — (1)Mateo (1998); (2) Irwin & Hatzidimitriou (1995); (3) Odenkirchen et al. (2001); (4) Wilkinson et al. (2004); (5) Walker et al. (2006).

Table 2. Parameters of King models for dSph galaxies

Galaxy	$\frac{\Phi(0)}{\sigma^2}$	σ (km s ⁻¹)	r_c (kpc)	r_t (kpc)	M_{total} (10 ⁶ M _⊙)	M/L (M _⊙ /L _⊙)	$M(r < R_k)$ (10 ⁶ M _⊙)
Draco	4.3 ± 0.1	11 ± 1	0.182 ± 0.005	1.42 ± 0.04	34 ± 5	180 ± 30	28 ± 4
Ursa Minor	5.0 ± 0.6	18 ± 2	0.18 ± 0.02	1.7 ± 0.3	100 ± 20	500 ± 150	83 ± 28
Fornax	1.5 ± 0.1	23 ± 2	1.11 ± 0.05	2.84 ± 0.04	180 ± 20	11 ± 4	160 ± 50

Table 3. Parameters of luminosity profiles

	R_{max} (kpc)	a (L_{\odot} kpc $^{-3}$)	b (kpc $^{-1}$)	c (L_{\odot} kpc $^{-3}$)	d (kpc $^{-1}$)	N_a	χ^2	$ N_a - \chi^2 $ ($\sqrt{2N_a}$)
Draco	2.0	4.69×10^6	9.17	3.26×10^3	0.98	44	68	2.6
Ursa Minor	2.0	6.27×10^6	10.4	1.01×10^4	1.22	38	31	0.8
Fornax ^a	6.0	-4.21×10^7	4.79	4.21×10^7	3.55	66	95	2.5

^aWe perform the optimization with the constraint that the central density $a + c \geq 0$.

Table 4. Results from two-integral models of dwarf spheroidal galaxies

Mass model ^a	ΔLH	$\mathbf{X}\{1\}^b$	$\mathbf{X}\{2\}^c$	$M(r < R_k)^d$ ($10^6 M_\odot$)	$\bar{\Gamma}_V(r < R_k)^e$ ($M_\odot/L_{V,\odot}$)
Draco					
1	−0.3	180^{+140}_{-50}	$0.48^{+0.23}_{-0.12}$	73^{+24}_{-16}	480^{+160}_{-110}
2	0.0	16^{+26}_{-12}	$2.0^{+3.3}_{-1.0}$	60 ± 12	400 ± 80
3 ^f	−0.1	77 ± 8	$1.1^{+0.2}_{-0.5}$	72^{+24}_{-16}	480^{+160}_{-110}
4	−8.0	80^{+40}_{-20}	...	77^{+47}_{-27}	510^{+310}_{-180}
5	−13.7	420 ± 60	...	63 ± 9	420 ± 60
6	−36.8	38 ± 4	...	38 ± 4	250 ± 30
Ursa Minor					
1	0.0	140^{+50}_{-30}	$0.18^{+0.08}_{-0.04}$	93^{+23}_{-16}	580^{+140}_{-100}
2	−3.3	970^{+700}_{-600}	$0.20^{+0.13}_{-0.05}$	93^{+21}_{-16}	580^{+130}_{-100}
3	−4.2	22 ± 4	$1.8^{+0.2}_{-0.4}$	101^{+13}_{-17}	630^{+80}_{-110}
4	−20.0	22^{+11}_{-7}	...	100^{+55}_{-36}	630^{+340}_{-230}
5	−4.0	720 ± 60	...	150 ± 10	720 ± 60
6	−14.9	80 ± 9	...	80 ± 9	500 ± 60
Fornax					
1	0.0	660^{+370}_{-240}	$0.9^{+0.2}_{-0.3}$	340^{+90}_{-70}	25^{+7}_{-5}
2	−0.7	13^{+17}_{-7}	$2.2^{+1.4}_{-1.0}$	350^{+100}_{-90}	25^{+7}_{-6}
3	−1.3	19 ± 2	$1.4^{+0.2}_{-0.4}$	390^{+110}_{-80}	28^{+9}_{-6}
4	−9.7	20^{+9}_{-6}	...	500^{+450}_{-200}	36^{+33}_{-14}
5	−6.9	17 ± 3	...	240 ± 40	17 ± 3
6	−17.7	180 ± 30	...	180 ± 30	13 ± 2

^aModel: 1. isochrone, 2. NFW, 3. power-law, 4. constant density, 5. constant mass-to-light ratio, 6. black hole. See §2 for description of the models.

^bThe first parameter of mass distribution models: mass for isochrone and black hole models in units of $10^6 M_\odot$, density for NFW, power-law, and constant density models in units of $10^6 M_\odot \text{ kpc}^{-3}$, mass-to-light ratio for constant mass-to-light ratio model in units of $M_\odot/L_{V,\odot}$. See Equations (3)-(6) for definitions of the parameters.

^cThe second parameter of mass distribution models: radius for isochrone and NFW models in units of kpc, density exponent for power-law model.

^dMass interior to the limiting radius R_k of kinematic data. $R_k = 0.75$ kpc for Draco, 1.1 kpc for Ursa Minor and 2.5 kpc for Fornax.

^eThe average mass-to-light ratio within $r = R_k$.

^fThe arbitrary parameter r_0 (eq. 5) is chosen as 0.28 kpc for Draco, 0.6 kpc for Ursa Minor and 1.1 kpc for Fornax.

Table 5. Results from three-integral models of dwarf spheroidal galaxies^a

Mass model	ΔLH	$\mathbf{X}\{\mathbf{1}\}$	$\mathbf{X}\{\mathbf{2}\}$	$M(r < R_k)$ ($10^6 M_\odot$)	$\bar{\Gamma}_V(r < R_k)$ ($M_\odot/L_{V,\odot}$)
Draco					
1	−0.3	330^{+180}_{-160}	$0.51^{+0.08}_{-0.16}$	74^{+19}_{-16}	490^{+130}_{-110}
2	−0.3	26^{+25}_{-17}	$1.2^{+2.0}_{-0.5}$	58^{+20}_{-13}	380^{+130}_{-70}
3	0.0	81 ± 14	1.1 ± 0.4	77 ± 26	510 ± 170
4	−9.5	83^{+40}_{-30}	...	83^{+40}_{-30}	510^{+310}_{-180}
5	−5.2	370 ± 40	...	56 ± 6	370 ± 40
6	−31.9	29 ± 3	...	29 ± 3	190 ± 20
Ursa Minor					
1	−0.3	170 ± 50	$0.21^{+0.04}_{-0.08}$	105^{+29}_{-25}	660^{+180}_{-160}
2	−0.1	300^{+1100}_{-130}	$0.37^{+0.12}_{-0.19}$	114^{+28}_{-21}	710^{+180}_{-130}
3	0.0	30^{+7}_{-6}	1.4 ± 0.3	125^{+26}_{-22}	780^{+160}_{-130}
4	−16.4	22^{+11}_{-8}	...	100^{+56}_{-36}	630^{+350}_{-230}
5	−1.7	720 ± 60	...	115 ± 10	720 ± 60
6	−11.1	88 ± 9	...	88 ± 9	550 ± 60
Fornax					
1	−2.5	2100^{+600}_{-500}	$1.5^{+0.2}_{-0.3}$	520^{+90}_{-100}	38 ± 7
2	−0.1	$5.9^{+0.6}_{-0.3}$	4.0 ± 0.4	460^{+60}_{-80}	33^{+4}_{-6}
3	0.0	25^{+3}_{-7}	$1.3^{+0.2}_{-0.3}$	500^{+70}_{-40}	36^{+5}_{-3}
4	−13.0	22^{+11}_{-8}	...	550^{+530}_{-250}	40^{+39}_{-18}
5	−9.7	15 ± 2	...	210 ± 30	15 ± 2
6	−17.8	180 ± 40	...	180 ± 40	13 ± 3

^aDefinitions and units of all parameters are the same as those in Table 4

Table 6. Statistics of the best-fit models

Model	e_a	N_b	χ_v^2	$\frac{ \chi_v^2 - N_b }{(\sqrt{2N_b})}$	N_a	χ^2	$\frac{ \chi^2 - N_a }{(\sqrt{2N_a})}$
Draco							
King	0.0	10	54.3	9.9	44	108.5	6.9
$f(E, L_{z'})$	0.25	10	21.1	2.5	44	38.7	0.6
$f(E, L, L_{z'})$	0.30	10	21.0	2.4	44	32.2	1.3
Ursa Minor							
King	0.0	10	13.9	0.9	38	40.3	0.3
$f(E, L_{z'})$	0.35	10	6.3	0.8	38	53.2	1.7
$f(E, L, L_{z'})$	0.40	10	3.0	1.6	38	52.1	1.6
Fornax							
King	0.0	10	57.9	10.7	66	172.5	9.3
$f(E, L_{z'})$	0.15	10	13.1	0.7	66	39.9	2.3
$f(E, L, L_{z'})$	0.30	10	12.9	0.6	66	34.9	2.7